

# Enhanced Surface Superconductivity of Niobium by Zirconium Doping

Nathan S. Sitaraman<sup>1,¶</sup>, Zeming Sun,<sup>2,¶</sup> Benjamin L. Francis<sup>1,§</sup>, Ajinkya C. Hire,<sup>4,5,¶</sup>  
 Thomas Oseroff<sup>1,¶</sup>, Zhaslan Baraissov,<sup>6</sup> Tomas A. Arias,<sup>1,\*</sup> Richard G. Hennig,<sup>4,5,†</sup>  
 Matthias U. Liepe<sup>1,‡</sup>, David A. Muller,<sup>6</sup> and Mark K. Transtrum<sup>3,§</sup>  
 (Center for Bright Beams)

<sup>1</sup> Department of Physics, Cornell University, Ithaca, New York 14853, USA

<sup>2</sup> Cornell Laboratory for Accelerator-Based Sciences and Education, Cornell University, Ithaca, New York 14853, USA

<sup>3</sup> Department of Physics and Astronomy, Brigham Young University, Provo, Utah 84602, USA

<sup>4</sup> Department of Materials Science and Engineering, University of Florida, Gainesville, Florida 32611, USA

<sup>5</sup> Quantum Theory Project, University of Florida, Gainesville, Florida 32611, USA

<sup>6</sup> Department of Applied Physics, Cornell University, Ithaca, New York 14853, USA

(Received 22 August 2022; revised 30 May 2023; accepted 27 June 2023; published 28 July 2023)

Superconducting radio-frequency (SRF) cavities currently rely on niobium (Nb), and could benefit from a higher- $T_c$  surface, which would enable a higher operating temperature, lower surface resistance, and higher maximum fields. Surface zirconium (Zr) doping is one option for improvement, which has not previously been explored, likely because bulk alloy experiments showed only mild  $T_c$  enhancements of 1–2 K relative to Nb. Our *ab initio* results reveal a more nuanced picture: an ideal bcc Nb-Zr alloy would have  $T_c$  over twice that of niobium, but displacements of atoms away from the high-symmetry bcc positions due to the Jahn-Teller-Peierls effect almost completely eliminates this enhancement in typical disordered alloy structures. Ordered Nb-Zr alloy structures, in contrast, are able to avoid these atomic displacements and achieve higher calculated  $T_c$  up to a theoretical limit of 17.7 K. Encouraged by this, we tested two deposition methods: a physical-vapor Zr deposition method, which produced Nb-Zr surfaces with  $T_c$  values of 13.5 K, and an electrochemical deposition method, which produced surfaces with a possible 16-K  $T_c$ . An rf test of the highest- $T_c$  surface showed a mild reduction in BCS surface resistance relative to Nb, demonstrating the potential value of this material for RF devices. Finally, our Ginzburg-Landau theory calculations show that realistic surface doping profiles should be able to reach the maximum rf fields necessary for next-generation applications, such as the ground-breaking LCLS-II accelerator. Considering the advantages of Nb-Zr compared to other candidate materials such as Nb<sub>3</sub>Sn and Nb-Ti-N, including a simple phase diagram with relatively little sensitivity to composition, and a stable, insulating ZrO<sub>2</sub> native oxide, we conclude that Nb-Zr alloy is an excellent candidate for next-generation, high-quality-factor superconducting rf devices.

DOI: 10.1103/PhysRevApplied.20.014064

## I. INTRODUCTION

While higher- $T_c$  materials long ago supplanted niobium (Nb) in dc wire applications, this humble elemental superconductor (with transition temperature  $T_c = 9.2$  K)

remains the material of choice for rf surface applications [1–5] due to the relative ease of producing devices, which approach its fundamental limits of surface resistance and superheating field  $B_{sh}$  (the maximum magnetic field at which the Meissner state can be maintained). Higher- $T_c$  surfaces could push these limits further, potentially resulting in far more practical and cost-effective superconducting radio-frequency (SRF) cavities for particle accelerators, in particular. The need for cavities with a high quality factor (low surface resistance) as well as high accelerating gradient (limited by  $B_{sh} = 240$  mT for niobium) for next-generation particle accelerators has resulted in many efforts to improve Nb cavities, for example, by growing compound superconductors on the surface. Multilayer superconductors are expected to delay the onset of vortex penetration, leading to increased cavity efficiency

\*taa2@cornell.edu

†rhennig@ufl.edu

‡mul2@cornell.edu

§mktranstrum@byu.edu

¶These authors contributed equally.

at higher fields [6–8]. Candidate materials have included MgB<sub>2</sub> [9], NbN [10], Nb-Ti-N [11,12], and Nb<sub>3</sub>Sn [13–17]. However, this research has so far failed to approach the theoretical limits [18–21] of these materials due to the difficulty of growing them uniformly on the Nb surface and due to their considerably reduced coherence lengths of just a few nanometers, which make them far more sensitive than Nb to nanoscale defects [22,23].

In contrast, relatively little attention has been paid to the possibility of enhancing  $T_c$  and  $B_{sh}$  within the native bcc structure of Nb, likely due the perception of an only mild  $T_c$  enhancement for the best known bcc alloy candidate Nb-Zr ( $T_c = 10.8$  K) [24]. This would otherwise be a very attractive option; while A15 superconductors like Nb<sub>3</sub>Sn and rocksalt superconductors like Nb-Ti-N tend to exist in complicated binary or ternary phase diagrams with low- $T_c$  or normal-conducting phases nearby, bcc alloy systems such as Nb-Zr are relatively simple, with the Nb-rich half of the phase diagram completely free of low- $T_c$  phases [25–27]. Additionally, while Nb<sub>3</sub>Sn and Nb-Ti-N form complex surface oxides that may behave poorly under rf conditions [28,29], Zr doping facilitates the growth of a wide-band-gap ZrO<sub>2</sub> oxide layer, which is simpler than the Nb native oxide [30,31]. Specifically, while the Nb native oxide tends to contain a variety of oxygen-deficient phases that may absorb rf energy [32–34], the Zr native oxide tends to form very near the ideal ZrO<sub>2</sub> composition [35,36]. These advantages, as well as a potentially longer coherence length, could help Nb-Zr avoid quench-inducing defects, and could also help Nb-Zr reach the low residual (low-temperature limit) resistance values necessary for applications in quantum computing and particle detection [3,16].

To better understand the potential for SRF applications of the Nb-Zr alloy system, we begin with density-functional theory (DFT) and Eliashberg theory in the dilute limit, where the virtual crystal approximation (VCA) allows us to calculate a variety of superconducting properties. We confirm that the addition of Zr to Nb increases  $T_c$ , and potentially much more than had previously been observed in bulk Nb-Zr alloy experiments. We then switch from VCA to a supercell approach in order to directly account for lattice relaxation effects and better understand the potential for greatly enhanced  $T_c$ . With this approach, we find good agreement with the literature for random alloys at all concentrations, and we show that ordered alloy structures can surpass the limitations of the random alloy to reach notably higher  $T_c$  values.

Encouraged by these results, we synthesize Nb-Zr alloy surface layers of different Zr doping profiles using physical vapor and electrochemical methods and examine their material and rf superconducting properties. We find that the measured  $T_c$  meets or exceeds literature values for Nb-Zr random alloys, in agreement with our calculations. We show that the enhanced  $T_c$  likely translates to improved

performance under rf conditions by comparing the BCS resistance of the alloyed sample to that of a reference Nb sample.

Putting together the data from our DFT calculations and our experimental sample analysis, we use Ginzburg-Landau (GL) theory to investigate how Nb surfaces with different Zr doping profiles will affect the superheating field  $B_{sh}$ . Doping with Zr generally results in surface layers whose concentration of Zr varies with depth. Such material inhomogeneities are known to affect maximum rf fields [23], including  $B_{sh}$  (see also Ref. [7] for a phenomenological discussion of these effects). Previous studies of these effects have calculated  $B_{sh}$  for layered materials [37] and continuously varying impurity concentrations [38] using Eilenberger theory (which is valid for  $T \ll T_c$ ), and for spatial variations in  $T_c$  [39,40] using time-dependent GL theory (which is valid for  $T$  near  $T_c$ ). We expand on these studies by incorporating continuous spatial variations of multiple material properties simultaneously, and show that a realistic Zr-doping profile could nearly double  $B_{sh}$ . Taken together with potential gains in quality factor and operating temperature, the prospect of significantly increased maximum rf fields makes Zr doping a promising approach for many important applications.

## II. SUPERCONDUCTING PROPERTIES OF NB-ZR IN THE DILUTE LIMIT

We calculate the superconducting properties of Nb-Zr alloys in the dilute limit using VCA. We use QUANTUM ESPRESSO (QE) [41–43] to perform the DFT calculations. We use the Perdew-Burke-Ernzerhof [44] functional for the exchange-correlation energy and norm-conserving pseudopotentials [45,46]. We use the Methfessel-Paxton smearing scheme [47] to smear the electrons during lattice relaxation. The isotropic  $\alpha^2 F$  is calculated in QE with the tetrahedron method [48] using a  $q$  mesh of  $8 \times 8 \times 8$  and a  $k$  mesh of  $24 \times 24 \times 24$ . We use the EPW code (electron-phonon Wannier) [49,50] to solve the Migdal-Eliashberg equations for superconducting gap and critical temperature with the isotropic  $\alpha^2 F$  as an input.

To check the accuracy of VCA, we calculate the density of states (DOS) at the Fermi level using the VCA method and compare it with that calculated using supercells at 12.5 at%Zr and 25 at%Zr concentration (8 atom supercell cells). Only the lattice vectors of the supercells were relaxed, and the atoms were kept fixed on the high-symmetry sites. This constraint was applied to maintain consistency between VCA and supercell calculations. Moreover, allowing atoms to move away from the high symmetry tends to decrease the DOS at the Fermi level, especially at high concentrations, as shown in Sec. III. Comparing the DOS at the Fermi level calculated using VCA and supercell, Fig. 1(a), we find that the shape of the DOS between the two methods matches well, but VCA

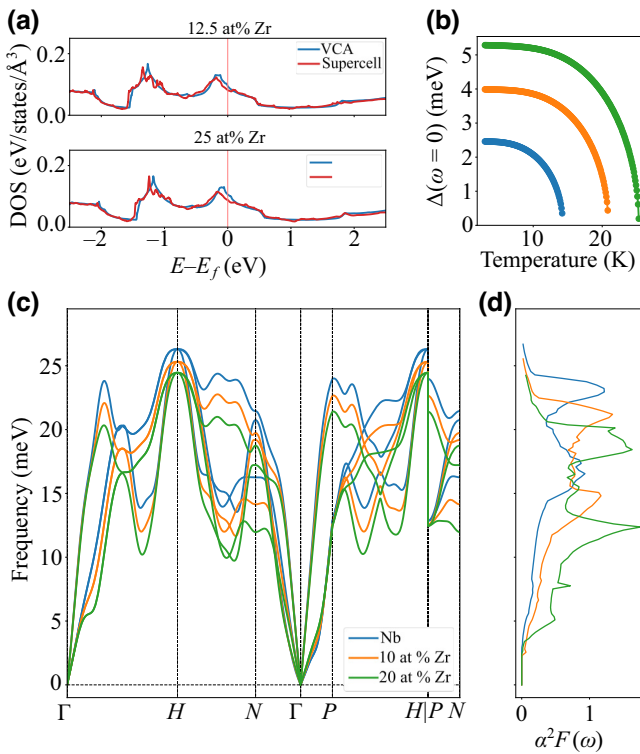


FIG. 1. (a) DOS at the Fermi level using the VCA and supercell methods. The upper plot is at 12.5 at%Zr and the lower plot is at 25 at%Zr concentration. (b) Superconducting gap as a function of temperature. (c) Calculated phonon dispersion and (d)  $\alpha^2 F$  of Nb-Zr alloys. The blue, orange, and green lines are for pure Nb, 10 at%Zr and 20 at%Zr, respectively. As Zr concentration increases, phonons at lower frequency couple strongly with electrons, increasing the electron-phonon coupling constant.

overestimates DOS at the Fermi level by 16% and 20% at 12.5 at%Zr and 25 at%Zr concentration, respectively. This is due to a slight shifting of the peaks near the Fermi level. We expect this overestimation of DOS in VCA calculations to be less of an issue while calculating superconducting properties at low Zr concentrations; for higher Zr concentrations, refer to Sec. III.

TABLE I. Calculated superconducting properties of Nb-Zr alloys using VCA and GL theory, including the electron-phonon coupling constant  $\lambda^e$  and the superconducting gap  $\Delta$ .  $T_c$  was calculated using the Allen-Dynes equation, Xie [51], and isotropic Eliashberg theory using  $\mu^* = 0.16$ .  $\lambda_L$  and  $B_c$  have been rescaled to match known values for Nb (Refs. [52] and [53], respectively), while the rescaling value for  $\xi$  was calculated via the GL relation  $\xi = \Phi_0/(2\pi\sqrt{2}B_c\lambda_L)$  [54] (where  $\Phi_0 \equiv h/2e$ ).

Composition	$\lambda^e$	$\Delta(4K)$ (meV)	$v_F$ (m/s)	$N(0)$ (states/eV/Å³)	$T_c^{AD}$ (K)	$T_c^{Xie}$ (K)	$T_c^{El}$ (K)	$\lambda_L$ (nm)	$\xi$ (nm)	$\kappa$	$B_c$ (mT)	$B_{sh}$ (mT)
Nb	1.13	2.4	$8.50 \times 10^5$	0.082	11.24	10.39	14.2	39.0	29.9	1.30	199	241
$Nb_{0.95}Zr_{0.05}$	1.30	3.0	$8.20 \times 10^5$	0.086	13.60	13.46	16.8	39.5	23.9	1.65	247	287
$Nb_{0.90}Zr_{0.10}$	1.69	4.0	$8.09 \times 10^5$	0.091	17.18	18.30	20.8	38.9	18.7	2.08	321	368
$Nb_{0.80}Zr_{0.20}$	2.37	5.3	$7.79 \times 10^5$	0.103	21.17	24.28	25.3	38.0	14.6	2.61	421	456
$Nb_{0.75}Zr_{0.25}$	2.85	5.8	$7.70 \times 10^5$	0.106	22.02	26.49	26.7	37.9	13.8	2.74	444	478

Table I shows the calculated superconducting properties for Zr concentrations ranging from 0 to 25%. The calculated  $T_c$  agrees well between the three methods used to calculate the critical temperature: Allen-Dynes [55], Xie [51], and isotropic Eliashberg. Figure 1(b) shows the isotropic superconducting gap as a function of temperature, from which the Eliashberg  $T_c$  is obtained as the temperature at which the gap goes to zero. As Zr concentration increases, so do the electron-phonon coupling constant, superconducting gap, and the  $T_c$  of the alloy. This increase in  $T_c$  can be attributed to softening of the phonons, as shown in Fig. 1(c), and an increase in the density of states at the Fermi level  $N(0)$ , which ultimately leads to stronger  $\alpha^2 F$  [Fig. 1(d)]. Note that our calculated  $T_c$ 's and superconducting gap values for pure Nb overestimate the experimental values of 9.23 K and 1.5 meV, respectively [56]. It has been suggested that including the effect of spin fluctuation is essential for estimating the  $T_c$  of Nb [57,58], which is not included in our calculations. Nevertheless, we expect that spin fluctuation will have little effect on the trends in the critical temperature and fields highlighted in Table I. Later in Sec. III, we account for spin fluctuations via an additive shift to the electron-phonon coupling for estimating the  $T_c$  of ordered Nb-Zr alloys.

### III. SUPERCONDUCTING PROPERTIES OF NB-ZR ALLOYS AT HIGHER ZR CONCENTRATIONS

Previous experimental studies of  $Nb_{1-n}Zr_n$  bcc random alloys have found moderately increased  $T_c$  and greatly increased upper critical field  $B_{c2}$  compared to Nb across a broad compositional range from  $n = 0$  to  $n = 0.5$  [24,27]. Alloys made with molybdenum (Mo), Nb's other fifth-row neighbor, have  $T_c$ 's that drop off quickly with increasing Mo concentration. This data (black dots in Fig. 2) is in qualitative agreement with the simple alloy theory originally used to describe bcc alloy superconductivity, namely that there is a universal  $d$ -band shape, and alloying simply shifts the position of the Fermi level by adding or removing  $d$ -band electrons, thus altering  $N(0)$  and therefore  $T_c$  [24,59]. Quantitatively, this effect is captured in our VCA

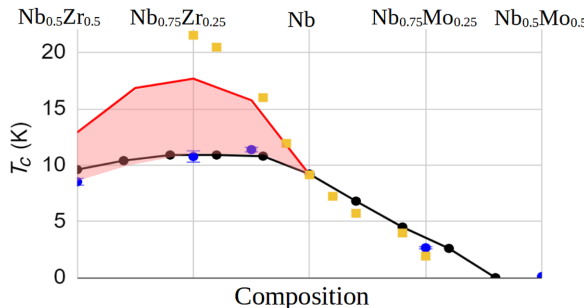


FIG. 2. Alloy  $T_c$  versus composition for experiment (black, Ref. [24]), VCA (yellow squares), random supercell theory (blue circles), and Jahn-Teller-Peierls stability limit (red).

calculations (yellow squares in Fig. 2), which show good agreement with experiment for Nb-Mo, but significantly overestimate  $T_c$  for Nb-Zr. This indicates that, while VCA may accurately describe Nb-Mo and dilute Nb-Zr alloys, it misses relevant nonlinear effects in the Nb-Zr system that alter the  $d$ -band shape and tend to lower  $T_c$ .

Exploration of the full compositional range of  $\text{Nb}_{1-n}\text{Zr}_n$ , therefore, requires an analysis of Nb-Zr, which accounts fully for the effects of Zr substitutions in the Nb lattice; for this we employ the supercell method. Specifically, for each  $n$ , we construct 48-atom supercells, substitute the required number of Nb atoms with Zr at random sites, and fully relax the structure, using the JDFTx software package with the PBE exchange-correlation functional and ultrasoft pseudopotentials [44,60,61]. Averaging the resulting DOS over multiple configurations at each composition yields an expected macroscopic  $N(0)$ . We then estimate  $T_c$  as a function of composition through the BCS  $N(0)$ - $T_c$  relationship, resulting in the “random alloy” predictions displayed by the blue dots in Fig. 2. We find quite good agreement with the random-alloy experiments for both Nb-Mo and Nb-Zr, indicating that our calculated  $N(0)$ -composition relationship correctly captures the nonlinear effects that determine  $T_c$  in Nb-Zr random alloys.

While material properties like those in Table I are not generally straightforward to compute for the random alloy (calculation of the phonon dispersion, in particular, is complicated by the large unit cell and lack of symmetries), we expect that most of them, like  $N(0)$ , will fall somewhere between the Nb value and the ideal virtual crystal alloy value. We thus expect, for example, that the increases in  $B_c$  and  $B_{sh}$  would be more modest for bulk random alloy samples and cavities than predicted, since most of the increase can be attributed to the predicted changes in  $T_c$  (roughly,  $B_{sh} \sim B_c \sim T_c$ ). The notable exception to this is the electron mean free path, which is extremely sensitive to composition in the random alloy. Based on defect-scattering calculations [31], we expect that it will drop from the clean-limit Nb value to less than 10 nm at 5% Zr composition, and to less than 5 nm at 10% Zr

composition. In conjunction with a depth-dependent doping profile, this would generally result in a sample with short mean free path and high  $T_c$  near the surface, and long mean free path and  $T_c$  approaching the Nb value further from the surface.

Examining our supercell calculations, we find that, for atoms at their unrelaxed, ideal bcc locations, the electronic DOS for Nb-Zr alloys resemble that of Nb with a rigid band shift, similar to what would be found in VCA. However, we find that the minimum-energy atomic coordinates diverge significantly from the ideal bcc locations in a way that significantly reduces  $N(0)$ . This final, reduced  $N(0)$  value varies only modestly with composition up to 50% Zr, explaining the modest variations that are observed in  $T_c$ . Figure 3(a) illustrates this relaxation effect for the 50/50 Nb-Zr random alloy, where the initially large DOS peak near the Fermi level essentially vanishes. Moreover, consistent with our observation that simple alloy theories work well for Nb-Mo, Fig. 3(b) shows this relaxation effect to be absent in the Nb-Mo system.

Fundamentally, the Nb-Zr alloy minimizes its energy by lowering the energies of occupied electronic states near the Fermi level, resulting in a reduced  $N(0)$ . This relaxation does not occur in Nb-Mo, which has fewer states near the Fermi level, and thus less ability to lower its energy in this manner. The redistribution of electronic energy levels in Nb-Zr is accomplished by the relaxation of lattice degrees of freedom, i.e., by the movement of atoms away from their ideal lattice positions. This brings us to a key difference between random Nb-Zr alloys, which have been our focus so far, and ordered Nb-Zr alloys. It has been pointed out that the symmetries of highly ordered structures can effectively limit the degrees of freedom for

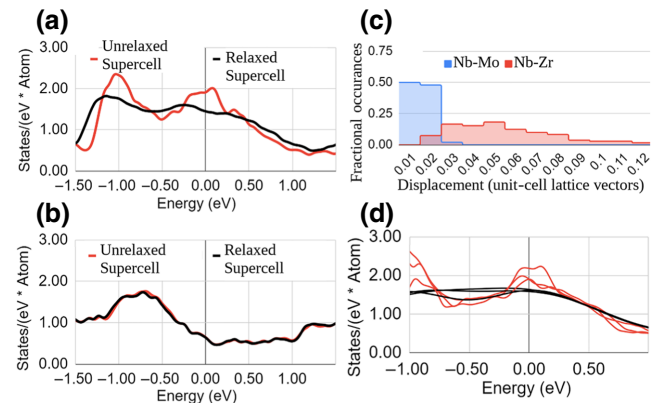


FIG. 3. Electronic DOS for 50/50 Nb-Zr (a) and Nb-Mo (b) random alloys before atomic relaxation (red) and after atomic relaxation (black). (c) Histogram of atomic displacements in 50/50 Nb-Zr (red) and Nb-Mo (blue) alloys. (d) DOS curves for three different ordered 50/50 Nb-Zr alloys before (red) and after (black) applying electronic state energy broadening to reduce  $N(0)$  and stabilize the structure.

lattice relaxation [55]. In our case, this could result in a crystal with electronic structure similar to the VCA or the unrelaxed-random-alloy electronic structure and thus a much higher  $T_c$ . It may be possible to grow such an ordered alloy in a low-temperature thin-film process such as those often employed in SRF cavity production.

We estimate the maximum attainable  $T_c$  of an ordered Nb-Zr alloy of a given composition as follows. We note that the same force, which drives ionic displacements in the Nb-Zr random alloy, tends to break the symmetries of ordered Nb-Zr structures. Indeed, this Jahn-Teller-Peierls effect has been proposed as a driving force for bcc phase instability in binary alloys, including Nb-Zr [62]. The magnitude of this driving force is directly related to the  $N(0)$  of the unrelaxed structure, which we can tune artificially by broadening the electronic state energies in our calculations. We then determine the limiting value of  $N(0)$  beyond which the Jahn-Teller-Peierls instability causes the structure to break its symmetry and relax to a lower-symmetry state with reduced  $N(0)$ . Figure 3(d), for example, shows the result of this process for three high-symmetry structures at the same Zr concentration of  $n = 0.5$ , showing that they all exhibit very similar  $N(0)$  just before the onset of the instability. Finally, this stability-limited Fermi-level DOS can be used to determine the limiting  $T_c$  as a function of composition through BCS theory. Figure 2 (“Jahn-Teller-Peierls stability limit” curve) displays the results of the above process. We generally expect that the  $T_c$  values for  $\text{Nb}_{1-n}\text{Zr}_n$  will all lie within the pink shaded region, between the random alloy result and the limiting Jahn-Teller-Peierls value for any special, ordered structure. For example, an Eliashberg calculation for a specific ordered structure at  $n = 0.25$  gives an electron-phonon coupling constant  $\lambda^e = 1.93$  compared to a value of  $\lambda^e = 1.18$  for Nb. To estimate the corresponding  $T_c$  enhancement, we use the Allen-Dynes formula with  $\mu^* = 0.1$  and an additive shift in the  $\lambda^e$  parameter to account for spin fluctuations and match the experimental  $T_c$  of bulk Nb [55,63]. This yields a  $T_c$  of 15.7 K for the ordered  $n = 0.25$  alloy, close to our predicted stability limit of 17.7 K. This prediction represents an additional 50% enhancement over the random alloy  $T_c$ , similar to what we indeed observe in our experiments.

#### IV. EXPERIMENTAL VERIFICATION

To validate our theoretical predictions, we measured the superconducting properties and rf performance of different Nb-Zr surface profiles. The samples were prepared by *e*-beam evaporation of a Zr target on electropolished Nb surfaces under a base pressure of  $1.3 \times 10^{-6}$  torr, followed by thermal annealing at 600 and 1000°C for 10 h with a ramp-up rate of 5°C/min under a vacuum of  $2 \times 10^{-7}$  torr, and a subsequent etch in 2% HF for 30 min. The initial film thickness and postannealing condition

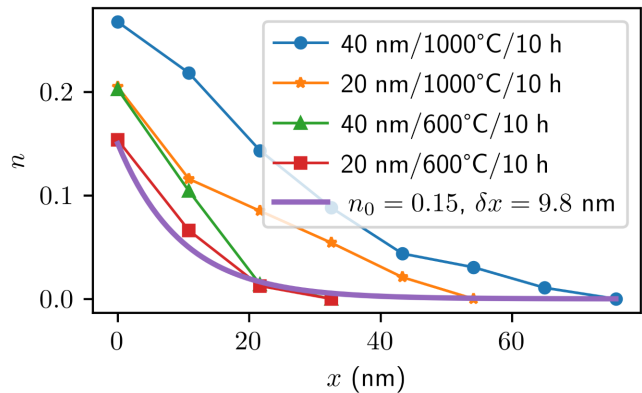


FIG. 4. Zr concentration  $n$  versus depth  $x$  for Nb-Zr samples prepared with various initial Zr film thicknesses and annealing conditions. Also shown is an example profile  $n(x)$  [Eq. (4)], which roughly approximates one of the measured samples. We predict that an SRF cavity with this type of Nb-Zr profile on its surface could have  $B_{\text{sh}} \approx 275$  mT (see Fig. 6).

were varied to modify the surface Zr atomic concentration. The sample preparation method and annealing process are detailed in Ref. [64].

X-ray photoelectron spectroscopy reveals a surface Zr concentration of 15–27 at.% Zr on the evaporation-based samples (Fig. 4), along with significant oxygen concentrations. X-ray diffraction [Fig. 5(a)] indicates that substitutional Zr doping is achieved, as evidenced by the doping peaks at lower diffraction angles compared to a Nb cubic reference. Zr’s and Nb’s bcc lattice parameters are 0.354 and 0.330 nm, respectively [65]. Based on Vegard’s law, these doping peaks are induced by lattice enlargement when Zr dopants are incorporated into the cubic structure. Furthermore, the HF etch eliminates the hexagonal Zr phases that formed on the surface region after annealing. The hexagonal  $\alpha$  and  $\omega$  phases have low  $T_c$ ’s of 0.7 and 4 K, respectively [27,66], so avoiding these hexagonal phases is critical to obtaining high  $T_c$ . Additionally, the only oxide detected is  $\text{ZrO}_2$ . Note that some normal-conducting oxides appearing on the conventional Nb surface are relevant to the loss [32–34,67], whereas a dielectric like  $\text{ZrO}_2$  is ideal for SRF applications due to its wide band gap.

Resistivity drop measurements using a Physical Property Measurement System under the ac transport mode demonstrate a  $T_c$  of up to 13.5 K for evaporation-based samples that were annealed at 600°C for 10 h. Moreover, flux expulsion measurements indicate, albeit with some caution [64], that the electrochemically synthesized samples have a higher  $T_c$  of 16 K. Notably, the 13.5- and 16-K  $T_c$  values are significantly higher than the literature-reported 11-K  $T_c$  for Nb-Zr bulk alloys [27] and the 10.5-K  $T_c$  measured in sputtered Nb-Zr thin films [68], as well as the 11-K  $T_c$  measured in the 1000°C annealed

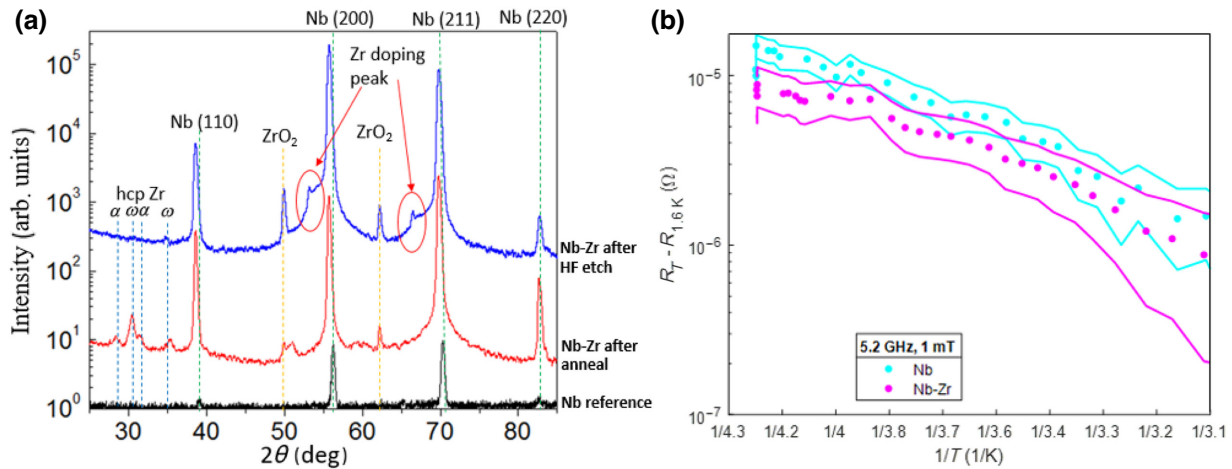


FIG. 5. Structural and superconducting properties of Nb-Zr samples. (a) X-ray diffraction pattern for evaporation-based samples annealed at 600°C for 10 h and subsequently etched with HF. (b) Comparison of BCS surface resistance before and after Nb-Zr alloying.

samples in this work. It is possible that the lower annealing temperature of 600°C favors an ordered alloy structure with an unusually high  $T_c$ . For more details on the resistivity drop and flux expulsion measurements, refer to Ref. [64].

To assess the use of Nb-Zr alloys for SRF accelerator applications, we used an electrochemical recipe with  $ZrF_4/LiF$  in an ionic liquid to scale up the alloying process to produce a 12.7-cm plate compatible with the Cornell sample test cavity [69]. The electrochemical optimization is detailed in Ref. [64]. Indeed, as shown in Fig. 5(b), after Nb-Zr alloying, the 5.2 GHz low-field BCS surface resistance trends lower, which is consistent with the expected benefit of the high  $T_c$  of the Nb-Zr material. This rf demonstration of Nb-Zr alloys establishes an alternative direction for SRF cavities with high  $T_c$  and low surface resistance. As we now show, these cavities also have the potential for high superheating fields.

## V. GL PREDICTIONS OF $B_{sh}$

To calculate  $B_{sh}$ , we employ GL theory to simulate Nb-Zr alloys in cavity surface layers using the data from Table I. The appeal of GL theory for such simulations is its ability to accommodate continuous spatial variations in material parameters. Although GL theory is *quantitatively* valid only for temperatures near  $T_c$ , the *qualitative* behavior it predicts, particularly the functional dependencies of various quantities, is still correct at low temperatures in many cases of interest. The necessary corrections to obtain quantitative predictions are usually constant numerical factors and rescalings, such as those noted in Refs. [54] and [70]. We, therefore, proceed to use GL theory to predict  $B_{sh}$  and other quantities of interest at zero temperature

by rescaling our results to match known values for Nb, which allows us to focus on predicting how these quantities change as Zr is added.

The main object of GL theory is the free energy density  $\mathcal{F}$  of the system [54,71,72], which includes both an expansion in a superconducting order parameter  $\psi$  (with phenomenological coefficients  $\alpha$ ,  $\beta$ , and  $\gamma$ ) and a contribution from the total magnetic field  $\mathbf{B} = \mathbf{B}_a - \nabla \times \mathbf{A}$ , where  $\mathbf{B}_a$  is the applied field and  $\mathbf{A}$  is the magnetic vector potential:

$$\mathcal{F} = \alpha|\psi|^2 + \frac{\beta}{2}|\psi|^4 + \gamma|(-i\hbar\nabla - 2e\mathbf{A})\psi|^2 + \frac{B^2}{2\mu_0}. \quad (1)$$

$B_{sh}$  is the value of  $|\mathbf{B}_a|$  at which the superconducting Meissner state becomes unstable.

For clean, homogeneous superconductors,  $N(0)$ ,  $T_c$ , and the Fermi velocity  $v_F$  can be used to calculate  $\alpha$ ,  $\beta$ , and  $\gamma$  [71,72]:

$$\alpha = \frac{N(0)}{T_c}(T - T_c), \quad \beta = \frac{7\zeta(3)N(0)}{8\pi^2 k_B^2 T_c^2}, \quad \gamma = \beta \frac{v_F^2}{6}. \quad (2)$$

These coefficients, in turn, are related to the London penetration depth  $\lambda_L$ , coherence length  $\xi$ , and thermodynamic critical field  $B_c$ :

$$\lambda_L^2 = \frac{\beta}{8\mu_0 e^2 |\alpha| \gamma}, \quad \xi^2 = \hbar^2 \frac{\gamma}{|\alpha|}, \quad B_c = |\alpha| \sqrt{\frac{\mu_0}{\beta}}. \quad (3)$$

We use Eqs. (2) and (3) to calculate  $\lambda_L$ ,  $\xi$ , the GL parameter  $\kappa \equiv \lambda_L/\xi$ , and  $B_c$ , all at  $T = 0$ , for each of the compositions in Table I (rescaling to match known values for Nb, as previously noted).

We observe a favorable increase in  $B_c$  as Zr concentration increases. Note also that  $\lambda_L$  remains relatively constant while  $\kappa$  increases noticeably. This suggests that the lower critical field,  $B_{c1} \sim \ln \kappa / \lambda_L^2$  [54], also increases as Zr is added, which is particularly encouraging for rf cavity applications because cavities suffer quenches at  $B_{c1} < B < B_{sh}$ .

We use the linear stability analysis described in Ref. [19] to calculate  $B_{sh}$  at  $T = 0$  for each of the compositions in Table I. This represents a theoretical maximum value, from which we expect real cavities to deviate, e.g., due to inhomogeneities, such as the depth-varying concentrations of Zr shown in Fig. 4.

We simulate such inhomogeneous superconductors by treating the coefficients  $\alpha$ ,  $\beta$ , and  $\gamma$  as local quantities that vary spatially with material composition. We derive continuous functions  $\alpha(x)$ ,  $\beta(x)$ , and  $\gamma(x)$  for this purpose as follows. First, we consider a concentration profile  $n(x)$  in which Zr concentration  $n$  falls off exponentially with depth  $x$  in the material from a surface value  $n_0$  on a scale set by  $\delta x$ :

$$n(x) = n_0 e^{-x/\delta x} \quad (4)$$

(see Fig. 4). We then interpolate the values of  $N(0)$ ,  $T_c^{\text{AD}}$ , and  $v_F$  in Table I for intermediate concentrations  $n$  to obtain  $N(0;x)$ ,  $T_c(x)$ , and  $v_F(x)$ . Finally, we compose these with Eq. (2) to obtain  $\alpha(x)$ ,  $\beta(x)$ , and  $\gamma(x)$ .

We calculate  $B_{sh}$  at  $T = 0$  for various choices of  $n_0$  and  $\delta x$ ; results are shown in Fig. 6. In all cases,  $B_{sh}$  increases as the total Zr content is increased, consistent with the improvements in other superconducting properties listed in Table I. In Sec. III, we noted that our VCA calculations captured in Table I likely overestimate  $T_c$  as Zr concentration increases; we expect our predictions of  $B_{sh}$  to be similarly optimistic since  $B_{sh} \sim B_c \sim T_c$  [see [19] and Eqs. (2) and (3)].

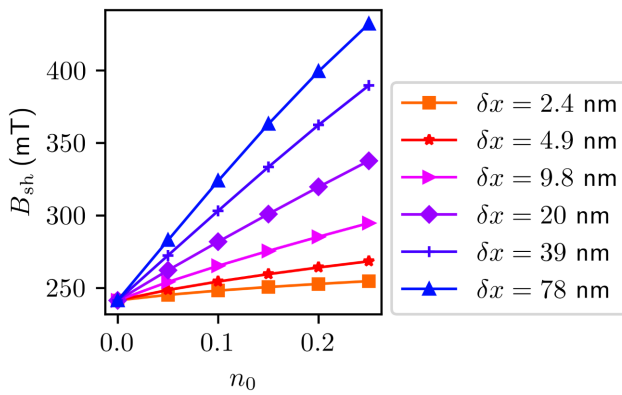


FIG. 6. Calculated  $B_{sh}$  at  $T = 0$  of Nb-Zr surface layers with varying compositions [see Eq. (4)], rescaled consistent with Table I.

## VI. CONCLUSION

In summary, we have proposed and demonstrated an alternative type of SRF surface via Nb-Zr alloying that enables (1) a high  $T_c$  of 13.5–16 K that minimizes energy dissipation and cryogenic costs; (2) potential enhancement of  $B_{sh}$  to upwards of 400 mT, which would allow approximately 95 MV/m accelerating gradients (currently, the best Nb cavities can only reach 45–50 MV/m [73–75]). Optimization of our initial recipe will aim to improve the uniformity of the high- $T_c$  layer and minimize possible contamination during the electrochemical process, while also considering the role of sample history and processing temperature on trapped flux [76–78]. Steps will be taken with the specific goal of reducing the residual resistance of the surface and making Nb-Zr competitive with Nb at typical SRF operating temperatures of 2 K and below. At higher temperatures, where the BCS resistance dominates, we find an excellent match between theoretical and experimental results, which show an improved  $T_c$  after Zr is incorporated into the Nb lattice and a lower surface resistance. Our theoretical predictions provide a viable road map to further tune and improve  $T_c$  and  $B_{sh}$ . Overall, we have demonstrated that Nb-Zr alloys promise to be an alternative, feasible technology for accelerator physics.

## ACKNOWLEDGMENTS

A.H. and R.H. performed the VCA calculations. N.S.S. and T.A.A. performed the supercell alloy calculations and thank Michelle Kelley and Ravishankar Sundararaman for helpful conversations. Z.S., T.O., Z.B., D.A.M., and M.U.L. completed the experimental verification, including material growth, characterization, and rf performance evaluation. Z.S. acknowledges Dr. Darrah K. Dare and Katrina Howard for experimental assistance. B.L.F. and M.K.T. did the GL predictions of  $B_{sh}$ . All authors revised the paper. This work made use of the Cornell Center for Materials Research Shared Facilities, which are supported through the NSF MRSEC program (DMR-1719875) and was performed in part at the Cornell NanoScale Facility, an NNCI member supported by NSF Grant No. NNCI-2025233. This work was supported by the U.S. National Science Foundation under Award No. PHY-1549132, the Center for Bright Beams.

- 
- [1] S. Kang, A. Goyal, J. Li, A. A. Gapud, P. M. Martin, L. Heatherly, J. R. Thompson, D. K. Christen, F. A. List, M. Paranthaman, and D. F. Lee, High-performance high- $T_c$  superconducting wires, *Science* **311**, 1911 (2006).
  - [2] M. Suenaga and W. B. Sampson, Superconducting properties of multifilamentary Nb<sub>3</sub>Sn made by a new process, *Appl. Phys. Lett.* **20**, 443 (1972).
  - [3] A. Romanenko, R. Pilipenko, S. Zorzetti, D. Frolov, M. Awida, S. Belomestnykh, S. Posen, and A. Grassellino,

- Three-Dimensional Superconducting Resonators at  $T < 20$  mK with Photon Lifetimes up to  $\tau = 2$  s, *Phys. Rev. Appl.* **13**, 034032 (2020).
- [4] H. S. Padamsee, Superconducting radio-frequency cavities, *Annu. Rev. Nucl. Part. Sci.* **64**, 175 (2014).
- [5] H. Padamsee, 50 years of success for SRF accelerators—a review, *Supercond. Sci. Technol.* **30**, 053003 (2017).
- [6] A. Gurevich, Enhancement of rf breakdown field of superconductors by multilayer coating, *Appl. Phys. Lett.* **88**, 012511 (2006).
- [7] T. Kubo, Multilayer coating for higher accelerating fields in superconducting radio-frequency cavities: A review of theoretical aspects, *Supercond. Sci. Technol.* **30**, 023001 (2016).
- [8] A. Gurevich, Theory of rf superconductivity for resonant cavities, *Supercond. Sci. Technol.* **30**, 034004 (2017).
- [9] T. Tan, M. A. Wolak, X. Xi, T. Tajima, and L. Civale, Magnesium diboride coated bulk niobium: A new approach to higher acceleration gradient, *Sci. Rep.* **6**, 35879 (2016).
- [10] C. Z. Antoine, M. Aburas, A. Four, F. Weiss, Y. Iwashita, H. Hayano, S. Kato, T. Kubo, and T. Saeki, Optimization of tailored multilayer superconductors for RF application and protection against premature vortex penetration, *Supercond. Sci. Technol.* **32**, 085005 (2019).
- [11] M. C. Burton, M. R. Beebe, K. Yang, R. A. Lukaszew, A.-M. Valente-Feliciano, and C. Reece, Superconducting NbTiN thin films for superconducting radio frequency accelerator cavity applications, *J. Vac. Sci. Technol. A* **34**, 021518 (2016).
- [12] Z. Sun, M. Liepe, T. Oseroff, and X. Deng, in *Proceedings of 20th International Conference on RF Superconductivity* (JACoW Publishing, East Lansing, MI, USA, 2021), p. 662.
- [13] S. Posen, M. Liepe, and D. Hall, Proof-of-principle demonstration of  $\text{Nb}_3\text{Sn}$  superconducting radiofrequency cavities for high  $Q_0$  applications, *Appl. Phys. Lett.* **106**, 082601 (2015).
- [14] S. Posen and D. L. Hall,  $\text{Nb}_3\text{Sn}$  superconducting radiofrequency cavities: fabrication, results, properties, and prospects, *Supercond. Sci. Technol.* **30**, 033004 (2017).
- [15] S. Posen, J. Lee, D. N. Seidman, A. Romanenko, B. Tenny, O. Melnychuk, and D. Sergatskov, Advances in  $\text{Nb}_3\text{Sn}$  superconducting radiofrequency cavities towards first practical accelerator applications, *Supercond. Sci. Technol.* **34**, 025007 (2021).
- [16] A. Berlin, S. Belomestnykh, D. Blas, D. Frolov, A. J. Brady, C. Braggio, M. Carena, R. Cervantes, M. Checchin, and C. Contreras-Martinez *et al.*, Searches for new particles, dark matter, and gravitational waves with SRF cavities, [arXiv:2203.12714](https://arxiv.org/abs/2203.12714).
- [17] Z. Sun, Z. Baraissov, L. Shpani, R. Porter, Y. Shao, T. Oseroff, M. Thompson, D. Muller, and M. Liepe, Smooth, homogeneous, high-purity  $\text{Nb}_3\text{Sn}$  RF superconducting films by seed-free electrochemical synthesis, [arXiv:2302.02054](https://arxiv.org/abs/2302.02054).
- [18] G. Catelani and J. P. Sethna, Temperature dependence of the superheating field for superconductors in the high- $\kappa$  London limit, *Phys. Rev. B* **78**, 224509 (2008).
- [19] M. K. Transtrum, G. Catelani, and J. P. Sethna, Superheating field of superconductors within Ginzburg-Landau theory, *Phys. Rev. B* **83**, 094505 (2011).
- [20] F. P. Lin and A. Gurevich, Effect of impurities on the superheating field of type-II superconductors, *Phys. Rev. B* **85**, 054513 (2012).
- [21] T. Kubo, Superfluid flow in disordered superconductors with dynes pair-breaking scattering: Depairing current, kinetic inductance, and superheating field, *Phys. Rev. Res.* **2**, 033203 (2020).
- [22] H. Padamsee, K. Shepard, and R. Sundelin, Physics and accelerator applications of RF superconductivity, *Annu. Rev. Nucl. Part. Sci.* **43**, 635 (1993).
- [23] H. Padamsee, The science and technology of superconducting cavities for accelerators, *Supercond. Sci. Technol.* **14**, R28 (2001).
- [24] J. K. Hulm and R. D. Blaisher, Superconducting solid solution alloys of the transition elements, *Phys. Rev.* **123**, 1569 (1961).
- [25] A. Godeke, A review of the properties of  $\text{Nb}_3\text{Sn}$  and their variation with A15 composition, morphology and strain state, *Supercond. Sci. Technol.* **19**, R68 (2006).
- [26] C. Benvenuti, P. Chiggiato, L. Parrini, and R. Russo, Production of niobium-titanium nitride coatings by reactive diffusion for superconducting cavity applications, *Nucl. Instrum. Methods Phys. Res., Sect. B: Beam Interactions with Materials and Atoms* **124**, 106 (1997).
- [27] J. M. Corsan, I. Williams, J. A. Catterall, and A. J. Cook, Superconductor transition temperatures of zirconium-niobium alloys, *J. Less-Common Metals* **15**, 437 (1968).
- [28] M. D. Henry, S. Wolfley, T. Young, T. Monson, C. J. Pearce, R. Lewis, B. Clark, L. Brunke, and N. Misset, Degradation of superconducting Nb/NbN films by atmospheric oxidation, *IEEE Trans. Appl. Supercond.* **27**, 1 (2017).
- [29] H. Ihara, Y. Kimura, H. Okumura, K. Senzaki, and S. Gonda, in *Advances in Cryogenic Engineering Materials: Volume 30* (Springer US, 1984), p. 589.
- [30] W. D. Klopp, D. J. Maykuth, C. T. Sims, and R. I. Jaffee, Oxidation and contamination reactions of niobium and niobium alloys, Tech. Rep. (Battelle Memorial Inst., Columbus, Ohio, 1959).
- [31] N. S. Sitaraman, Ph.D. thesis, Cornell University, 2022.
- [32] A. Gurevich and T. Kubo, Surface impedance and optimum surface resistance of a superconductor with an imperfect surface, *Phys. Rev. B* **96**, 184515 (2017).
- [33] C. Müller, J. H. Cole, and J. Lisenfeld, Towards understanding two-level-systems in amorphous solids: Insights from quantum circuits, *Rep. Prog. Phys.* **82**, 124501 (2019).
- [34] A. Romanenko and D. I. Schuster, Understanding Quality Factor Degradation in Superconducting Niobium Cavities at Low Microwave Field Amplitudes, *Phys. Rev. Lett.* **119**, 264801 (2017).
- [35] I. Bespalov, M. Datler, S. Buhr, W. Drachsel, G. Rupprechter, and Y. Suchorski, Initial stages of oxide formation on the Zr surface at low oxygen pressure: An in situ FIM and XPS study, *Ultramicroscopy* **159**, 147 (2015), 1st International Conference on Atom Probe Tomography and Microscopy.
- [36] M. Gerosa, C. E. Bottani, L. Caramella, G. Onida, C. Di Valentini, and G. Pacchioni, Defect calculations in semiconductors through a dielectric-dependent hybrid DFT functional: The case of oxygen vacancies in metal oxides, *J. Chem. Phys.* **143**, 134702 (2015).

- [37] T. Kubo, Superheating fields of semi-infinite superconductors and layered superconductors in the diffusive limit: structural optimization based on the microscopic theory, *Supercond. Sci. Technol.* **34**, 045006 (2021).
- [38] V. Ngampruetikorn and J. A. Sauls, Effect of inhomogeneous surface disorder on the superheating field of superconducting rf cavities, *Phys. Rev. Res.* **1**, 012015 (2019).
- [39] A. R. Pack, J. Carlson, S. Wadsworth, and M. K. Transtrum, Vortex nucleation in superconductors within time-dependent Ginzburg-Landau theory in two and three dimensions: role of surface defects and material inhomogeneities, *Phys. Rev. B* **101**, 144504 (2020).
- [40] J. Carlson, A. Pack, M. K. Transtrum, J. Lee, D. N. Seidman, D. B. Liarte, N. S. Sitaraman, A. Senanian, M. M. Kelley, J. P. Sethna *et al.*, Analysis of magnetic vortex dissipation in Sn-segregated boundaries in Nb<sub>3</sub>Sn superconducting RF cavities, *Phys. Rev. B* **103**, 024516 (2021).
- [41] P. Giannozzi, S. Baroni, N. Bonini, M. Calandra, R. Car, C. Cavazzoni, D. Ceresoli, G. L. Chiarotti, M. Cococcioni, I. Dabo *et al.*, QUANTUM ESPRESSO: A modular and open-source software project for quantum simulations of materials, *J. Phys.: Condens. Matter* **21**, 395502 (2009).
- [42] P. Giannozzi, O. Baseggio, P. Bonfà, D. Brunato, R. Car, I. Carnimeo, C. Cavazzoni, S. de Gironcoli, P. Delugas, F. F. Ruffino *et al.*, Quantum ESPRESSO toward the exascale, *J. Chem. Phys.* **152**, 154105 (2020).
- [43] P. Giannozzi, O. Andreussi, T. Brumme, O. Bunau, M. Buongiorno Nardelli, M. Calandra, R. Car, C. Cavazzoni, D. Ceresoli, M. Cococcioni *et al.*, Advanced capabilities for materials modelling with quantum ESPRESSO, *J. Phys.: Condens. Matter* **29**, 465901 (2017).
- [44] J. P. Perdew, K. Burke, and M. Ernzerhof, Generalized Gradient Approximation Made Simple, *Phys. Rev. Lett.* **77**, 3865 (1996).
- [45] D. R. Hamann, Optimized norm-conserving Vanderbilt pseudopotentials, *Phys. Rev. B* **88**, 085117 (2013).
- [46] M. Schlipf and F. Gygi, Optimization algorithm for the generation of ONCV pseudopotentials, *Comput. Phys. Commun.* **196**, 36 (2015).
- [47] M. Methfessel and A. T. Paxton, High-precision sampling for Brillouin-zone integration in metals, *Phys. Rev. B* **40**, 3616 (1989).
- [48] M. Kawamura, Y. Gohda, and S. Tsuneyuki, Improved tetrahedron method for the Brillouin-zone integration applicable to response functions, *Phys. Rev. B* **89**, 094515 (2014).
- [49] F. Giustino, M. L. Cohen, and S. G. Louie, Electron-phonon interaction using Wannier functions, *Phys. Rev. B* **76**, 165108 (2007).
- [50] S. Poncé, E. Margine, C. Verdi, and F. Giustino, EPW: Electron-phonon coupling, transport and superconducting properties using maximally localized Wannier functions, *Comput. Phys. Commun.* **209**, 116 (2016).
- [51] S. R. Xie, Y. Quan, A. C. Hire, B. Deng, J. M. DeStefano, I. Salinas, U. S. Shah, L. Fanfarillo, J. Lim, J. Kim, G. R. Stewart, J. J. Hamlin, P. J. Hirschfeld, and R. G. Hennig, Machine learning of superconducting critical temperature from Eliashberg theory, *Npj Comput. Mater.* **8**, 0 (2022).
- [52] B. W. Maxfield and W. McLean, Superconducting penetration depth of niobium, *Phys. Rev.* **139**, A1515 (1965).
- [53] D. Finnemore, T. Stromberg, and C. Swenson, Superconducting properties of high-purity niobium, *Phys. Rev.* **149**, 231 (1966).
- [54] M. Tinkham, *Introduction to Superconductivity* (Courier Corporation, Mineola, NY, 2004).
- [55] P. B. Allen and R. C. Dynes, Transition temperature of strong-coupled superconductors reanalyzed, *Phys. Rev. B* **12**, 905 (1975).
- [56] A.-M. Valente-Feliciano, Superconducting RF materials other than bulk niobium: A review, *Supercond. Sci. Technol.* **29**, 113002 (2016).
- [57] K. Tsutsumi, Y. Hizume, M. Kawamura, R. Akashi, and S. Tsuneyuki, Effect of spin fluctuations on superconductivity in V and Nb: A first-principles study, *Phys. Rev. B* **102**, 214515 (2020).
- [58] S. K. Bose, Electron-phonon coupling and spin fluctuations in 3D and 4D transition metals: Implications for superconductivity and its pressure dependence, *J. Phys.: Condens. Matter* **21**, 025602 (2008).
- [59] J. Bardeen, L. N. Cooper, and J. R. Schrieffer, Theory of superconductivity, *Phys. Rev.* **108**, 1175 (1957).
- [60] R. Sundararaman, K. Letchworth-Weaver, K. A. Schwarz, D. Gunceler, Y. Ozhabes, and T. A. Arias, JDFTx: Software for joint density-functional theory, *SoftwareX* **6**, 278 (2017).
- [61] K. F. Garrity, J. W. Bennett, K. M. Rabe, and D. Vanderbilt, Pseudopotentials for high-throughput DFT calculations, *Comput. Mater. Sci.* **81**, 446 (2014).
- [62] B. Feng and M. Widom, Band structure theory of the bcc to hcp Burgers distortion, *Phys. Rev. B* **98**, 174108 (2018).
- [63] J. Bekaert, A. Aperis, B. Partoens, P. M. Oppeneer, and M. V. Milošević, Advanced first-principles theory of superconductivity including both lattice vibrations and spin fluctuations: The case of FeB<sub>4</sub>, *Phys. Rev. B* **97**, 014503 (2018).
- [64] Z. Sun, T. Oseroff, Z. Baraissov, D. Dare, K. Howard, B. Francis, A. Hire, N. Sitaraman, T. Arias, M. Transtrum *et al.*, ZrNb(CO) RF superconducting thin film with high critical temperature in the theoretical limit, *Adv. Electron. Mater.* **9**, 2300151 (2023).
- [65] G. B. Thompson, R. Banerjee, S. A. Dregia, and H. L. Fraser, Phase stability of bcc Zr in Nb/Zr thin film multilayers, *Acta Mater.* **51**, 5285 (2003).
- [66] B. T. Wang, P. Zhang, H. Y. Liu, W. D. Li, and P. Zhang, First-principles calculations of phase transition, low elastic modulus, and superconductivity for zirconium, *J. Appl. Phys.* **109**, 063514 (2011).
- [67] Z. Sun, Z. Baraissov, C. Dukes, D. Dare, T. Oseroff, M. Thompson, D. Muller, and M. Liepe, Surface oxides, carbides, and impurities on RF superconducting Nb and Nb<sub>3</sub>Sn: A comprehensive analysis, [arXiv:2305.02467](https://arxiv.org/abs/2305.02467).
- [68] P. Koorevaar, W. Maj, P. H. Kes, and J. Aarts, Vortex-lattice transition in superconducting Nb/NbZr multilayers, *Phys. Rev. B* **47**, 934 (1993).
- [69] T. Oseroff, M. Liepe, and Z. Sun, in *Proceedings of 20th International Conference on RF Superconductivity* (JACoW Publishing, East Lansing, MI, USA, 2021), p. 357.

- [70] A. Suter, E. Morenzoni, N. Garifianov, R. Khasanov, E. Kirk, H. Luetkens, T. Prokscha, and M. Horisberger, Observation of nonexponential magnetic penetration profiles in the Meissner state: A manifestation of nonlocal effects in superconductors, *Phys. Rev. B* **72**, 024506 (2005).
- [71] N. Kopnin, *Theory of Nonequilibrium Superconductivity* (Oxford University Press, Oxford, England, 2001), Vol. 110.
- [72] P.-G. De Gennes and P. A. Pincus, *Superconductivity of Metals and Alloys* (CRC Press, Boca Raton, FL, 2018).
- [73] R. Geng, G. Eremeev, H. Padamsee, and V. Shemelin, in *2007 IEEE Particle Accelerator Conference (PAC)* (IEEE, Albuquerque, NM, 2007), p. 2337.
- [74] T. Kubo, Y. Ajima, H. Inoue, K. Umemori, Y. Watanabe, and M. Yamanaka, in *Proceedings of IPAC2014* (Dresden, Germany, 2014), p. 2519.
- [75] A. Grassellino, A. Romanenko, Y. Trenikhina, M. Checchin, M. Martinello, O. Melnychuk, S. Chandrasekaran, D. Sergatskov, S. Posen, A. Crawford *et al.*, Unprecedented quality factors at accelerating gradients up to  $45 \text{ MVm}^{-1}$  in niobium superconducting resonators via low temperature nitrogen infusion, *Supercond. Sci. Technol.* **30**, 094004 (2017).
- [76] A. Romanenko, A. Grassellino, A. C. Crawford, D. A. Sergatskov, and O. Melnychuk, Ultra-high quality factors in superconducting niobium cavities in ambient magnetic fields up to 190 mG, *Appl. Phys. Lett.* **105**, 234103 (2014).
- [77] S. Huang, T. Kubo, and R. L. Geng, Dependence of trapped-flux-induced surface resistance of a large-grain Nb superconducting radio-frequency cavity on spatial temperature gradient during cooldown through  $T_c$ , *Phys. Rev. Accel. Beams* **19**, 082001 (2016).
- [78] S. Posen, M. Checchin, A. C. Crawford, A. Grassellino, M. Martinello, O. S. Melnychuk, A. Romanenko, D. A. Sergatskov, and Y. Trenikhina, Efficient expulsion of magnetic flux in superconducting radiofrequency cavities for high Q applications, *J. Appl. Phys.* **119**, 213903 (2016).